Mathematical Biosciences and Engineering

MBE, 20(6): 9728–9758.
DOI: 10.3934/mbe.2023427
Received: 04 December 2022
Revised: 26 February 2023
Accepted: 12 March 2023
Published: 24 March 2023

http://www.aimspress.com/journal/MBE

*Research article*

# Low-dose sinogram restoration enabled by conditional GAN with cross-domain regularization in SPECT imaging

**Si Li, Limei Peng, Fenghuan Li* and Zengguo Liang***

School of Computer Science and Technology, Guangdong University of Technology, Guangzhou 510006, China

* **Correspondence:** Email: fhli20180910@gdut.edu.cn, zengguo.liang@outlook.com.

**Abstract:** In order to generate high-quality single-photon emission computed tomography (SPECT) images under low-dose acquisition mode, a sinogram denoising method was studied for suppressing random oscillation and enhancing contrast in the projection domain. A conditional generative adversarial network with cross-domain regularization (CGAN-CDR) is proposed for low-dose SPECT sinogram restoration. The generator stepwise extracts multiscale sinusoidal features from a low-dose sinogram, which are then rebuilt into a restored sinogram. Long skip connections are introduced into the generator, so that the low-level features can be better shared and reused, and the spatial and angular sinogram information can be better recovered. A patch discriminator is employed to capture detailed sinusoidal features within sinogram patches; thereby, detailed features in local receptive fields can be effectively characterized. Meanwhile, a cross-domain regularization is developed in both the projection and image domains. Projection-domain regularization directly constrains the generator via penalizing the difference between generated and label sinograms. Image-domain regularization imposes a similarity constraint on the reconstructed images, which can ameliorate the issue of ill-posedness and serves as an indirect constraint on the generator. By adversarial learning, the CGAN-CDR model can achieve high-quality sinogram restoration. Finally, the preconditioned alternating projection algorithm with total variation regularization is adopted for image reconstruction. Extensive numerical experiments show that the proposed model exhibits good performance in low-dose sinogram restoration. From visual analysis, CGAN-CDR performs well in terms of noise and artifact suppression, contrast enhancement and structure preservation, particularly in low-contrast regions. From quantitative analysis, CGAN-CDR has obtained superior results in both global and local image quality metrics. From robustness analysis, CGAN-CDR can better recover the detailed bone structure of the reconstructed image for a higher-noise sinogram. This work demonstrates the feasibility and

effectiveness of CGAN-CDR in low-dose SPECT sinogram restoration. CGAN-CDR can yield significant quality improvement in both projection and image domains, which enables potential applications of the proposed method in real low-dose study.

**Keywords:** SPECT; low-dose sinogram restoration; conditional generative adversarial network; cross-domain regularization; noise suppression

## 1. Introduction

Single-photon emission computed tomography (SPECT) is an effective imaging modality that has been widely used in oncology, for treatment monitoring and lesion malignancy evaluation, and in clinical diagnosis of cardiovascular diseases, bone scans, pulmonary perfusion imaging, lung ventilation imaging and regional cerebral blood flow tomography [1]. To obtain high-quality SPECT images for diagnosis, the standard dose of radiotracer or radiopharmaceutical is usually administered to the human body, thereby making the tissue-of-interest a source of gamma radiation. The single events due to gamma photons emitted from the tissue-of-interest can be recorded by a detector that rotates around the body. The collection of such emission events can then be sorted into a set of 2D projection data. Tomographic reconstruction of SPECT projection data can provide diagnostic information via estimates of the spatial and/or temporal distribution of radioactivity within the tissue-of-interest. The estimates are widely known as reconstructed images under appropriate representation. In the application of emission tomography, the absorption rate, scattering effect and background radiation all affect the quality of reconstructed images [2,3].

Despite the effectiveness of SPECT imaging in clinics, the ionizing radiation induced by its radiotracer poses a potential hazard to human health, especially an increased risk of cancer with a probability related to radiation dose. Clinically, a lower radiation dose can be achieved by reducing the activity of the administered radiotracer, which inevitably leads to lower photon counts recorded by the detector. Under these circumstances, the use of conventional image reconstruction methods to reconstruct projection data of low count rates usually yields images with increased Poisson noise, severe artifacts and decreased spatial resolution, which may degrade accuracy of diagnosis [4].

A tremendous amount of effort has been devoted to reducing radiation dose for SPECT imaging while maintaining the quality of reconstructed images. Model-based iterative reconstruction (MBIR) is one of the major handcrafted methods for reconstructing low-dose projection data or under-sampled k-space data [5–7]. MBIR methods have high mathematical interpretability, and they explicitly exploit the projective geometry and physical principle of data acquisition. Indeed, this category of reconstruction methods often develops proper regularization functionals to address the ill-posedness of image reconstruction problems and has greatly improved image quality over algebraic reconstruction techniques [8]. However, the traditional MBIR methods still suffer from relatively low performance (e.g., residual artifacts and decreased spatial resolution) due to their limited representation power. Moreover, the MBIR methods exhibit low efficiency and high bias, which may limit their clinical use.

In recent years, the development of deep learning technology has greatly promoted research on medical image reconstruction. In learning-based philosophy, the model parameters of either a traditional handcrafted optimization model or neural network architecture are typically optimized on a

given dataset. In the presence of a high-quality large-scale dataset, deep models can automatically learn the neural network parameters. In particular, the combination of handcrafted and learning-based methods is gaining more and more attention since it takes into account the advantages of both categories. At present, deep learning is mainly combined with handcrafted methods and applied to medical image reconstruction in the following three categories: network-model-based end-to-end reconstruction methods, post-learning (image-domain learning) methods and pre-learning (projection-domain learning) methods.

(1) Network-model-based end-to-end reconstruction methods generate high-quality cross-sectional images directly from the low-dose projection data. Some previous works [9,10] discussed end-to-end image reconstruction utilizing generic deep neural networks. For instance, Häggström et al. [9] presented an end-to-end positron emission computed tomography (PET) image reconstruction technique (DeepPET) based on a deep convolutional encoder-decoder network architecture, which took PET sinogram data as input and efficiently output high-quality, quantitative reconstructed images. Despite the lengthy training procedure, generic-network-based end-to-end reconstruction methods unbiasedly learn the inverse of the system model, the appropriate noise statistical model, and the regularization that best fits the characteristics of the input data, provided that the training samples are sufficiently abundant and diverse. However, the above category is often hampered in clinical applications where large-scale training samples are difficult to collect, and thus generic neural networks are intractable to train.

To tackle the above problem, algorithm unrolling has been proposed and extensively studied in recent studies [11–15]. Indeed, an algorithm unrolled network architecture is usually defined over a data flow graph, which is derived from the iteration procedures of the underlying reconstruction algorithm. In the training phase, all parameters originating from the algorithm iteration scheme are jointly learned in an end-to-end manner using training pairs of contaminated observation data and high-quality label images. In the testing phase, the algorithm unrolled network has lower computational overhead than its corresponding iterative algorithm, and adopts optimized parameters learned from the training samples for a specific reconstruction task. Unrolling methods, by expanding the capacity of iterative algorithms, have good potential in developing efficient, high-performance and relatively-high-generalizability network architectures from small-scale training data sets. However, compared to generic networks, unrolled networks usually exhibit customized structures, which may increase model bias and invalidate existing training schemes. In order to address both issues caused by unrolled networks, while reducing parameter dimensionality of end-to-end generic networks, there has been a large amount of research exploring two-stage image reconstruction, that is, performing intra-domain learning with lightweight generic networks and reconstructing images with conventional algorithms. Under these circumstances, generic networks are typically applied to post-processing of reconstructed images or pre-processing of projection data. In either case, generic networks only need to learn the statistical and regularization models while leaving the determination of the system matrix to handcrafted physical modeling. As a result, the above two categories allow utilization of lightweight networks and take advantage of both intra-domain learning and model-based handcrafted reconstruction.

(2) The post-learning methods perform network training after traditional image reconstruction and usually optimize the underlying network parameters on training pairs of low-dose reconstructed image (network input) and normal-dose reconstructed image (label). The aim of post-learning lies in removing artifacts and noise from the reconstructed images generated by an iterative reconstruction

method under low-dose acquisition mode. For example, Li et al. proposed a new 3D self-attentive learning scheme to solve the low-dose CT denoising problem [16]. The 3D self-attentive module uses the 3D volume of the CT image to capture the spatial information between CT slices. Han et al. [17] were among the first to adopt the approach of residual learning in sparse-view computed tomography (CT) reconstruction. Specifically, through a novel persistent homology analysis they showed that the manifold of image artifacts is topologically simpler than that of images, and they thus developed a deep residual learning architecture to estimate the image artifacts and further the artifact-free images via subtracting the artifacts from the input images. Following the lead of residual learning, Chen et al. [18] combined an autoencoder, deconvolution network and shortcut connection technique into a residual encoder-decoder convolutional neural network (CNN) with the aim of restoring low-dose CT images. Based on the encoder-decoder architecture, Zhang et al. [19] further applied cells of DenseNet to formulate the encoder module, where feature reuse can increase the depth of a neural network while greatly enhancing the expressive ability of the deep model.

The encoder-decoder architecture is capable of stepwise compressing the input image into a feature representation and then stepwise rebuilding the representation into a full dataset. This architecture is flexible for developing deep models that are effective in noise suppression, artifact removal and structure recovery for low-dose study. In particular, Ye et al. discovered that the encoder-decoder architecture emerges from the Hankel matrix decomposition [20] and thus further proposed a tight frame U-Net with orthogonal wavelet frame via adding additional high-frequency paths to the existing U-Net architecture [21]. The novel tight frame U-Net can effectively suppress blurring artifacts and exhibit better high-frequency recovery than the standard U-Net in sparse-view CT applications. In addition, the improved GoogLeNet [22] model with multi-scale convolution kernels has also been proven to be practical and effective for reducing artifacts in sparse-view CT reconstruction [23]. The category of post-learning methods provides a promising solution to the image artifact issues caused by sparse-view reconstruction. However, this category requires a large-scale training set of reconstructed images, and thus it is often used in conjunction with the low-computational-overhead analytic reconstruction algorithms (such as the filtered back-projection algorithm). Under these circumstances, the probabilistic model of noise and prior knowledge of the on image cannot be fully exploited.

The random noise in a low-dose sinogram may be amplified when reconstructed by the analytic reconstruction algorithm without prior knowledge. Such severely contaminated reconstructed images may increase the difficulty of neural network training in the post-learning category. On the contrary, pre-learning methods give a solution to remedy the above issue. Indeed, the pre-learning methods perform network training in the sinogram domain prior to image reconstruction, which decreases the training difficulty, as compared to image-domain training. Moreover, in the pre-learning category, image reconstruction only needs to be performed on the small-scale test set. Therefore, the high-computational overhead MBIR methods can be applied to the test stage to achieve further improved image quality.

(3) The pre-learning methods utilize pairs of low-dose and normal-dose projection data both in the sinogram domain for network training. In fact, the detected projection data in low-dose acquisition mode suffers from data deficiency. In recent years, there has been continuous exploration of sinogram pre-learning methods using deep neural networks to address data deficiency. For instance, the denoising or interpolation of CT or SPECT projection data was primarily implemented using the U-Net architecture combined with residual learning in [24–28]. In a similar fashion, Shiri et al. [29] used

a convolutional encoder-decoder architecture in the sinogram domain to generate gap-free PET sinograms. Furthermore, in [30], the U-Net architecture was used in combination with the long short-term memory network (LSTM) when processing the feature map in the decoding stage, so that the resulting deep model takes better consideration of the sequence property across adjacent projection angles in the sparse-view sinogram. In the other direction, with the advent of the generative adversarial network (GAN) [31], various deep models based on GAN architecture have also been applied to sinogram interpolation in medical imaging [32]. As an example, a sinogram super-resolution GAN model based on a residual-network generator was developed to generate high-resolution sinograms from the low-resolution counterparts in [33]. Later, Li et al. [34] proposed a variant of PatchGAN to recover the missing projection data when solving the reconstruction problem of limited angle CT. Similarly, [35] studied complementary limited-angle dual-energy computed tomography imaging using GAN. In general, the category of pre-learning methods learns the mappings from low-quality projection data to their high-quality counterparts, which facilitates unbiased image reconstruction and thus rarely relies on empirical prior knowledge.

Existing pre-learning methods for low-dose image reconstruction mainly address the super-resolution issue of sinograms; however, the denoising approaches of low-count-rate and thus high-noise sinograms are not fully explored. In the acquisition mode of reduced photon counts, the projection data exhibits increased Poisson noise and lower contrast. Such data degradations may be further amplified in the image domain due to the ill-posedness of the reconstruction problem. In order to improve the quality of SPECT reconstructed images under low-count-rate acquisition mode, while avoiding image-domain training, suppressing random noise in the projection domain and enhancing sinogram contrast by a pre-learning method constitute a useful approach.

The sinogram denoising problem usually meets two main challenges. First, the spatial variations, correlations and smoothness of sinograms differ from SPECT images, and thus the existing image-domain denoising models may not apply to the projection-domain study. Specifically, as compared to a reconstructed image, the sinogram usually exhibits lower contrast and more-distant correlation, since a local structure in the image usually corresponds to a specific global sinusoidal strip in the sinogram, and the overlapping of sinusoidal strips may degrade the sinogram contrast. Under these circumstances, a convolutional network architecture commonly used in the image domain requires more down-sampling layers or larger-sized convolution kernels to characterize globally-correlated information, which brings computational challenges to network training. Moreover, the traditional low-level uniform similarity metric may not provide satisfactory recovery of high-frequency sinusoidal features and sinogram contrast. Second, from the perspective of estimating effective information, sinogram super-resolution requires interpolating the missing information of the projection domain based on angular correlations of sinograms in a deterministic fashion; meanwhile, sinogram denoising needs to correct the noise-contaminated information through a handcrafted or learned statistical model. The very different mechanisms may limit the application of sinogram super-resolution methods in the denoising problem. Indeed, the random noise due to low-count-rate data acquisition may be magnified during the reconstruction process; hence, the development of appropriate noise suppression regularization is crucial to the sinogram denoising problem. As a result, there is a real need to specifically develop appropriate sinogram denoising methods, which can be accomplished via evaluating the feasibility of generic neural networks for this category of problems.

To address the aforementioned challenges, a conditional GAN [36] (CGAN)-based sinogram denoising model with cross-domain regularization (CGAN-CDR) is proposed with the aim of

generating high-quality sinograms for low-dose sinogram restoration in SPECT imaging. Then, a previously developed preconditioned alternating projection algorithm with total variation regularization (TV-PAPA) is adopted for image reconstruction from the restored sinogram. CGAN-CDR is composed of U-Net as the generator to generate fake normal-dose sinograms from low-dose SPECT sinograms and a patch discriminator to distinguish between generated sinograms and real normal-dose sinograms. This adversarial learning process occurs in conjunction with cross-domain regularization. The main contributions of this work are as follows: (1) The generator and discriminator in CGAN-CDR learn via an adversarial framework, which can better restore the detailed global sinusoidal features and recover the original contrast of the normal-dose sinogram. (2) The cross-domain regularization is performed in both projection and image domains, which can effectively ameliorate the issue of ill-posedness and serve as a constraint on the generator, thereby, helps achieve superior performance in noise suppression and contrast recovery. (3) Extensive numerical experiments are conducted to demonstrate the effectiveness of CGAN-CDR for low-dose sinogram restoration in SPECT imaging both qualitatively and quantitatively.

## 2. Methods

### *2.1 Problem formulation*

The purpose of this work is to reconstruct a high-quality image from a low-dose sinogram. This work is divided into two phases as shown in Figure 1. The first phase is sinogram preprocessing, which restores a high-quality sinogram from the low-dose counterpart. The second phase is reconstruction of restored test sinograms. Assume $x \in \mathbb{R}^m$ is the low-dose sinogram, $y_1 \in \mathbb{R}^m$ is the high-quality sinogram restored by a sinogram-domain mapping $F_1$, and $y_2 \in \mathbb{R}^d$ represents the reconstructed image of sinogram $y_1$ by a reconstruction algorithm $F_2$. The first phase can be expressed as

$$y_1 = F_1(x). \tag{1}$$

The second phase can be expressed as

$$y_2 = F_2(y_1). \tag{2}$$

In this work, the network model CGAN-CDR is proposed to restore high-quality sinograms in the first phase. CGAN-CDR is based on the CGAN framework, and a cross-domain regularization model in both the projection and image domains is developed to address the issues of sinogram degradation and reconstruction ill-posedness. Image reconstruction is an ill-posed problem in which even a slight oscillation in the high-quality sinogram may be amplified in the image domain. Therefore, we adopt the previously developed MBIR method TV-PAPA [6] for reconstruction of restored test sinograms with the aim of suppressing image-domain oscillation and preserving edges. In fact, TV-PAPA provides four interesting and useful features. First, it allows us to deal with the functions involved in the underlying optimization problem either through their proximity operators or through their gradients. Indeed, for non-differentiable functions, the proximity operator can be a powerful tool; however, for smooth functions, the gradient may be easier to implement. Second, the iterative scheme of PAPA does not require matrix inversion, which is an advantage when solving large-scale reconstruction problems

where matrix inversion can be quite expensive. Third, through the preconditioning technique, PAPA suggests that the search for the solution follows the direction of search in the classical expectation maximization algorithm, and it thus speeds up the original convergence rate. Finally, the number and size of filters used in total variation (TV) regularization are small, which further reduces the computational cost for each iteration.

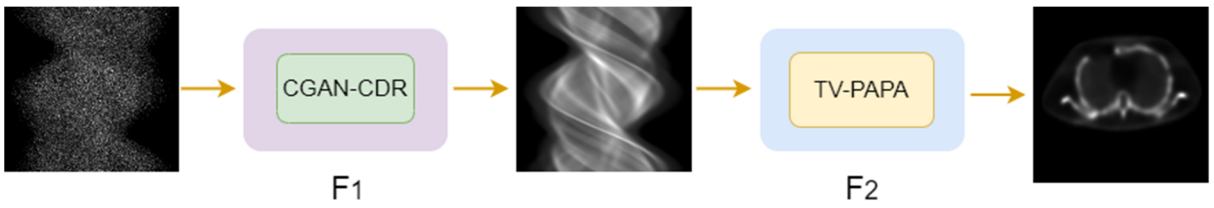


**Figure 1.** Framework of the proposed two-phase low-dose reconstruction method.

### *2.2 CGAN-CDR for sinogram restoration*

The proposed CGAN-CDR model is based on the CGAN framework and applied to the task of SPECT sinogram restoration. The proposed model consists of two neural networks that compete against each other. One neural network (U-Net) is the generator that generates fake normal-dose sinograms from the low-dose counterparts, while the other neural network (CNN) is the discriminator that evaluates the generated sinograms by comparing with the real normal-dose SPECT sinograms. This work takes advantage of CGAN, and modifies the original network structure so as to adapt to the underlying low-dose SPECT application. The overall network structure is shown in Figure 2. The low-dose sinogram $x$ is the input to generator network $G$, and $y$ denotes the normal-dose sinogram. In the following sections, we will describe the generator and discriminator for CGAN-CDR in detail.

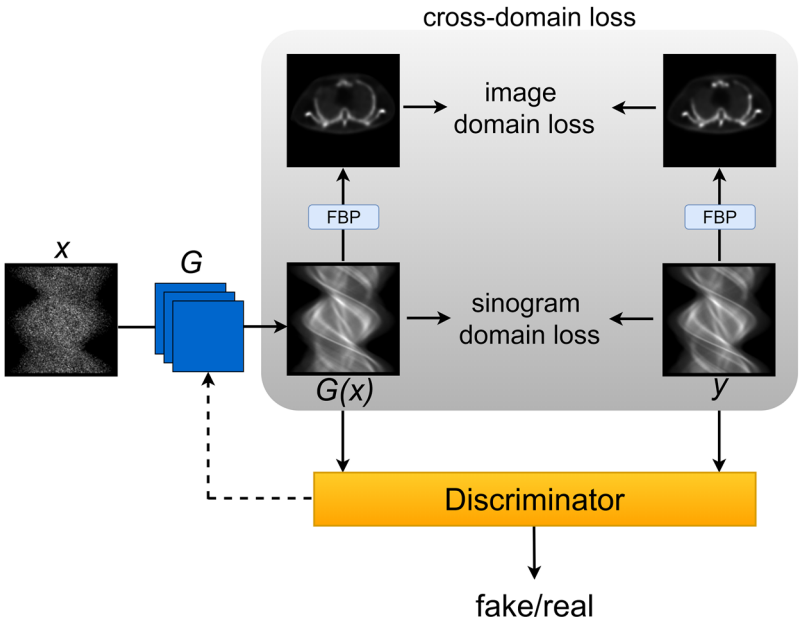


**Figure 2.** CGAN-CDR architecture for restoring high-quality sinogram from the low-dose counterpart.

The discriminator network learns to classify the fake (low-dose sinogram, generated sinogram by the generator network *G*) and real (low-dose sinogram, real normal-dose sinogram) tuples.

#### 2.2.1. Generator

SPECT sinograms typically exhibit fuzzy boundaries and relatively even gradients, which correspond to low-frequency information. Moreover, the recovery of high-frequency information in sinograms (e.g., the sinusoidal features and sinogram contrast) also requires careful consideration. U-Net is a typical encoder-decoder neural network [37]. It can combine low-frequency information at the bottom layers and high-frequency information at the top layers, which best suits the underlying scenario. Therefore, we adopted U-Net as the generator network and added skip connections to U-Net, enabling low-frequency and high-frequency information in the network to flow through all the modules. As a result, there can be a lot of low-level information sharing inputs and outputs [38]. U-Net is beneficial to global coherence of restored sinograms. The specific network structure of U-Net is shown in Figure 3, and it consists of 4 down-sampling modules and 4 up-sampling modules.

For input sinograms, down-sampling modules are first used for feature extraction. Each down-sampling module is composed of two stacked "Convolution-BatchNorm-LReLU" modules. Following a similar philosophy to that used in the visual geometry group network model [39], we set the size of the convolution kernel as $3 \times 3$ and the stride as 1 to achieve better sinogram feature extraction, and we adopt batch normalization processing to accelerate the convergence speed of the network. Meanwhile, the size of the sinogram is reduced to half of the original size by means of max pooling in each down-sampling module, which can enlarge the receptive field and reduce the computational cost.

After the bottleneck module, sinograms are recovered by up-sampling modules. In each up-sampling module, the sinogram size is enlarged to two times the original size by nearest neighbor algorithm, and then two convolution modules are used to retain the main information of the sinograms. Similarly, up-sampling modules also use batch normalization and leaky rectified linear unit (LReLU) to improve the speed and stability of network training.

We further set up symmetric skip connections between each pair of up-sampling module and the corresponding down-sampling module. High resolution information passes directly from the encoder to the decoder of the same height after concatenation operation. This can provide finer features for sinogram edges, so that the sinogram can be better restored. In order to adapt the generator, we expand the size of input sinograms from $120 \times 128$ to $128 \times 128$ by zero-filling to facilitate network training.

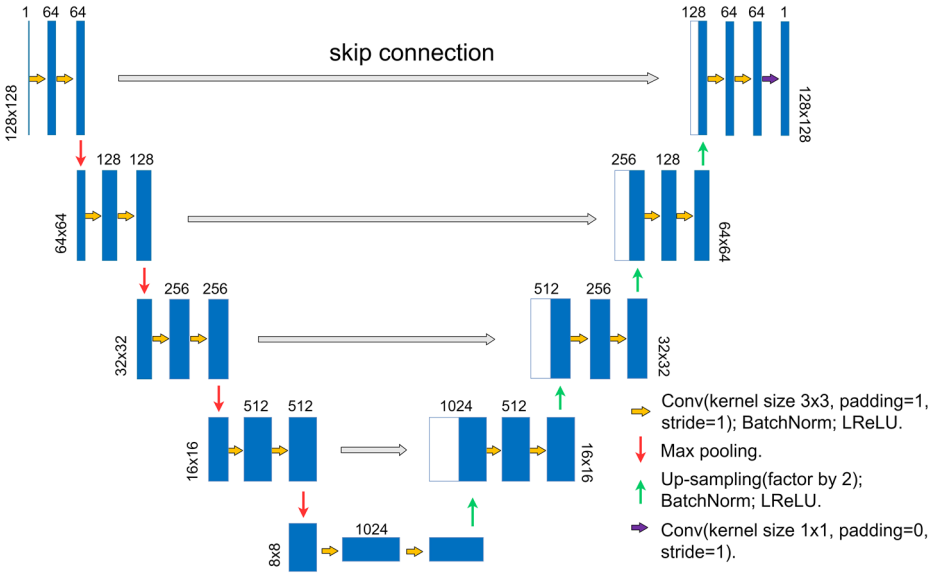


**Figure 3.** The structure of generator network.

### 2.2.2. Discriminator

A pixel-level similarity metric function, such as the $\ell^1$- or $\ell^2$-norm-based grey-level loss, can recover overall low-frequency information of the target image. However, the recovery of high-frequency information and the enhancement of image contrast remain challenging issues. According to Odena et al. [40], an adversarial network (the discriminator) potentially learns an adaptive similarity metric that can optimize for detailed features, edges and contrast in images beyond the low-level uniform similarity metric. With this lead, we exploit the discriminator network in PatchGAN [38] to capture and characterize the sinusoidal features within sinogram patches, since various patches in a sinogram exhibit different spatial variations and thus should be evaluated independently.

Unlike traditional GAN, where the discriminator outputs a single evaluation value for the whole sinogram, PatchGAN is accompanied by an additional convolution operation which captures and evaluates the detailed sinusoidal features in various sinogram patches. Indeed, after passing through sequential convolution modules, the underlying sinogram is further mapped to $N \times N$ evaluation matrix using an additional convolutional operation, instead of being fed into a fully connected layer. Each element in the $N \times N$ evaluation matrix represents the prediction result corresponding to a specific patch in the generated sinogram. The realistic prediction by the $N \times N$ evaluation matrix, instead of by a single value, can effectively characterize detailed features in local receptive fields and focus on more local regions. Finally, we average all $N \times N$ prediction results to provide the overall output of the underlying discriminator. In numerical simulation, we empirically determined the patch size to be $13 \times 13$. By discriminating various sinogram patches, the local sinusoidal features are effectively extracted, which facilitates the improvement of sinogram resolution and contrast.

The inputs of the underlying discriminator are pairs of generated and label sinograms. The discriminator has six modules, and its structure is shown in Figure 4. The first module consists of a 4×4 convolution operation with a stride of 2. Both the second and third modules consist of a 4×4 convolution operation with a stride of 2 and a Leaky ReLU followed by batch normalization. The fourth and fifth modules consist of a $4 \times 4$ convolution operation with a stride of 1 and the

aforementioned Leaky ReLU. The last module remains a 4×4 convolution operation with a stride of 1. In summary, given input sinogram pairs, the discriminator network *D* employs a series of "Convolution-BatchNorm-LReLU" modules to extract high-level features in the sinogram domain.

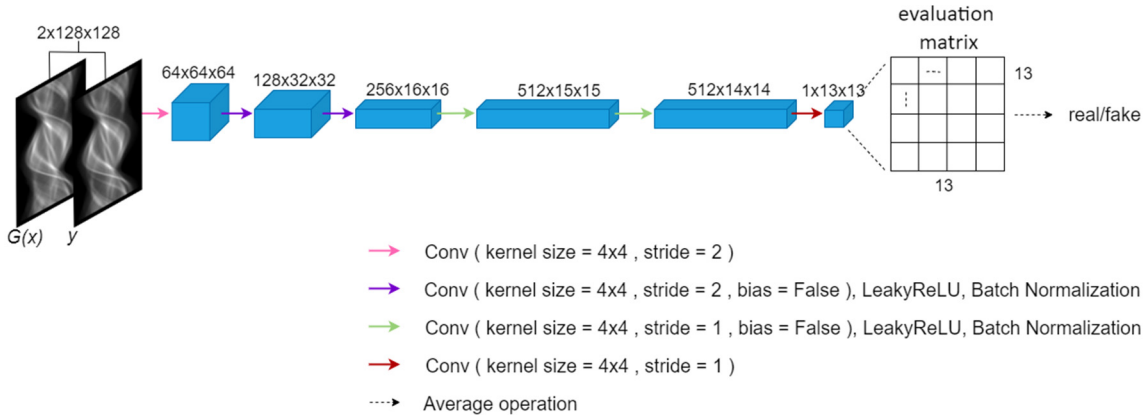


**Figure 4.** The structure of discriminator network *D* with details of convolutional modules. The variable *y* denotes the real normal-dose sinogram, and *G(x)* denotes the generated sinogram by generator network *G*.

### 2.2.3. Loss function

In this work, the total loss function consists of three terms. The first term is the adversarial loss function, which prompts the generator network to achieve the desired manifold projection and produce sinograms with accurate details. The second term is the projection-domain consistency loss function, which directly constrains the generator via penalizing the difference between the generator output and the label sinogram in a component-wise sense. The projection-domain loss can help recover accurate contrast between sinusoidal waves in the sinogram restoration process. The third term is the image-domain consistency loss function, which imposes a similarity constraint on the reconstructed images of generated and label sinograms. The image-domain loss can address the issue of ill-posedness and serves as an indirect constraint on the generator. Indeed, sinogram noise may be amplified during an ill-posed reconstruction process; therefore, an effective noise-suppressed and artifact-reduced image-domain regularization can in turn enhance the quality of generated sinograms. We refer to projection-domain and image-domain losses collectively as the cross-domain regularization function. Finally, the minimax optimization problem for the CGAN-CDR can be defined as follows:

$$\min_{G}\max_{D}[\ell_{\text{adv}}(G,D)+\omega\ell_{\text{sin}}(G)+\lambda\ell_{\text{image}}(G)]. \tag{3}$$

(1) Adversarial loss $\ell_{\text{adv}}(G,D)$

The CGAN-CDR considers the situation that the generator *G* and discriminator *D* are conditioned on low-dose sinogram $x$. The generator *G* generates the corresponding sinogram *G(x)*, which is used to confuse the discriminator *D*. The learning of generator *G* makes the discriminator *D* have difficultly determining whether *G(x)* is the corresponding normal-dose sinogram *y*. The discriminator *D* learns progressively to distinguish between the generated sinogram *G(x)* and the normal-dose sinogram *y*.

This adversarial training prompts the generated sinogram *G(x)* to obey the empirical distribution in the projection domain and to exhibit high-quality normal-dose characteristics both in sinusoidal details and contrast. The adversarial loss can be formulated as follows:

$$\ell_{\text{adv}}(G,D) = E_{x\sim P_{data}(x),y\sim P_{data}(y)}[\log(D(x,y))] + E_{x\sim P_{data}(x)}[\log(1-D(x,G(x)))]. \tag{4}$$

(2) Projection-domain loss $\ell_{\text{sin}}(G)$

The overall accuracy and noise suppression performance of generated sinograms, compared to the corresponding normal-dose sinograms (i.e., labels), are critical to reconstruction quality, since the estimation error due to the generator network model and the random noise due to the low-dose data acquisition scenario may be magnified during the reconstruction process. Therefore, a direct penalty on the generator network is necessary to improve the overall training accuracy and to enforce desired smoothness and spatial variation of the generated sinograms. While the adversarial loss can facilitate the recovery of detailed features and contrast in the target sinograms, a pixel-level similarity metric function tends to better denoise low-count-rate and hence low-contrast, high-noise sinograms and to directly improve the consistency between generated sinograms and labels. Note that a sparsity constraint on the difference between generated and normal-dose sinograms can further improve sinogram accuracy in the low-contrast scenario. As a result, we may take advantage of both adversarial loss and sparsity-promoting $\ell^1$-norm similarity metric, thereby generating restored sinograms of low noise, accurate contrast and high accuracy. Indeed, the $\ell^1$-norm-based projection-domain similarity loss function can be formulated as follows:

$$\ell_{\text{sin}}(G) = E_{x\sim P_{data}(x),y\sim P_{data}(y)}[\| y - G(x) \|_1], \tag{5}$$

where $y$ represents the normal-dose sinogram, and *G(x)* represents the restored sinogram by generator network *G* from the low-count-rate input sinogram *x*. Loss function (5) penalizes the disparity in the sinogram domain in a component-wise fashion. This projection-domain loss is a function of generator *G*, which together with the adversarial loss (4) guarantees a superior performance in recovery of detailed features and contrast and in suppression of severe noise.

(3) Image-domain loss $\ell_{\text{image}}(G)$

The ill-posedness of SPECT image reconstruction magnifies the estimation error and Poisson noise in the restored sinogram, leading to critical artifacts, severe noise and even structural deformation of the reconstructed image. In order to directly and effectively ameliorate the above image degradations, we propose to penalize the difference between reconstructed images of generated and label sinograms, which in turn further improves the sinogram accuracy. Common reconstruction algorithms consist of the filtered back-projection (FBP) algorithm and iterative reconstruction algorithm. The iterative reconstruction algorithm is computationally expensive, which may invalidate the overall network training. Hence, we choose the reconstructed images after FBP to formulate the image-domain similarity loss function. In this manner, the quality of restored sinograms and quality of reconstructed images are simultaneously improved and mutually promoted. In particular, the $\ell^1$-norm-based image-domain similarity loss function is defined as follows:

$$\ell_{\text{image}}(G) = E_{x\sim P_{data}(x),y\sim P_{data}(y)}[\| R^{-1}(g * G(x)) - R^{-1}(g * y)\|_1]. \quad (6)$$

Here, *G(x)* denotes the output of generator *G* from the low-count-rate sinogram *x*, *y* denotes the normal-dose sinogram, *g* denotes the Ram-Lak filter used in the FBP algorithm, and $R^{-1}$ denotes the inverse Radon transform.

The generator and discriminator networks are updated in the way of alternating gradient descent. The detailed training procedure is shown in Algorithm 1.

**Algorithm 1: CGAN-CDR training procedure**

**Initialization:** hyper-parameters $\lambda = 0.6, \omega = 0.01, lr = 0.0002, \beta_1 = 0.5, \beta_2 = 0.999$, the number of total epochs $N_{epoch} = 1000$, the batch size $n = 16$, the discriminator parameter $\theta_d$ and generator parameter $\theta_g$ are initialized by random Gaussian distribution $N(0, 0.02^2)$.

1: **for** num_epoch = 0, ..., $N_{epoch}$ **do**

2: Sample a batch of low-dose sinogram $\{x^{(i)}\}_{i=1}^{n}$ and the corresponding normal-dose sinogram $\{y^{(i)}\}_{i=1}^{n}$

3: **for** *i*=1, …, *n,* **do**

4: $\ell_{\text{adv}}^{(i)}(D) \leftarrow \log(D(x^{(i)}, y^{(i)})) + \log(1 - D(x^{(i)}, G(x^{(i)})))$

5: **end for**

6: Update $D: \theta_d \leftarrow \text{Adam}(\nabla_{\theta_d} \frac{1}{n}\sum_{i=1}^{n} \ell_{\text{adv}}^{(i)}(D), \theta_d, lr, \beta_1, \beta_2)$

7: **for** *i*=1, …, *n,* **do**

8: $L^{(i)}(G) \leftarrow \lambda \ell_{\text{image}}\left(G\left(x^{(i)}\right)\right) + \omega \ell_{\sin}\left(G\left(x^{(i)}\right)\right) + \log(1 - D(x^{(i)}, G(x^{(i)})))$

9: **end for**

10: Update $G: \theta_g \leftarrow \text{Adam}(\nabla_{\theta_g} \frac{1}{n}\sum_{i=1}^{n} L^{(i)}(G), \theta_g, lr, \beta_1, \beta_2)$

11: **end for**

### *2.3. TV-PAPA*

The reconstruction problem can be formulated via the penalized maximum likelihood criterion, which is realized by maximizing the sum of the log-likelihood function of activity distribution vector *f* and the negative penalty term. In particular, the SPECT reconstruction optimization model reads:

$$\hat{f} \coloneqq \arg\min_{f\geq 0}\{\langle Af, \mathbf{1}\rangle - \langle \ln(Af + \gamma), u\rangle + \lambda\varphi(Bf)\}, \quad (7)$$

where $A \in \mathbb{R}^{m\times d}$ is the system matrix, and $\gamma \in \mathbb{R}^m$ is the vector of background counts. The composite function $\varphi \circ B$ is a real-valued energy function, and $\lambda$ is a positive regularization parameter. Specifically, when the regularization term $\lambda\varphi \circ B$ reduces to TV, the regularization matrix *B* is specified as a first-order difference matrix. For the convenience of exposition, we consider a typical SPECT image as a $p \times p \times q$ hypermatrix and treat this hypermatrix as a vector in $\mathbb{R}^{p^2q}$ in such a way that the *ijk*th entry of the image matrix corresponds to the $(i + (j-1)p + (k-1)p^2)$th component of the vector. In the current context, we reserve *d* for $p^2q$. In TV regularization, *B* is a $3d \times d$ matrix defined, through the identity matrix *I*, the backward difference matrix *D* and the notion

of Kronecker tensor product $\otimes$, as

$$B := \begin{bmatrix} I_q \otimes I_p \otimes D_p \\ I_q \otimes D_p \otimes I_p \\ D_q \otimes I_p \otimes I_p \end{bmatrix} \text{ with } D := \begin{bmatrix} 0 & & \\ -1 & 1 & \\ & \ddots & \ddots \\ & & -1 \ 1 \end{bmatrix}.$$

The detailed construction of matrix $B$ and TV regularization model may be referred to in [6]. The data fidelity function $\langle A \cdot, \mathbf{1} \rangle - \langle \ln(A \cdot + \gamma), u \rangle$, denoted by $F$, is the Kullback-Leibler (KL) divergence.

With the above notation, the reconstruction algorithm PAPA [6] has the following iterative scheme:

$$\begin{cases} \hbar^{(k)} := P_+\left(f^{(k)} - S\nabla F\left(f^{(k)}\right) - \mu S B^{\mathrm{T}} b^{(k)}\right), \\ b^{(k+1)} = \left(I - \mathrm{prox}_{(\lambda/\mu)\varphi}\right)\left(b^{(k)} + B\hbar^{(k)}\right), \\ f^{(k+1)} = P_+\left(f^{(k)} - S\nabla F\left(f^{(k)}\right) - \mu S B^{\mathrm{T}} b^{(k+1)}\right). \end{cases} \tag{8}$$

In scheme (8), $S$ is a positive-definite preconditioning matrix of $d \times d$, $\mu$ is a positive parameter, and $b^{(k)}$ is the dual iterate defined in the domain of the first-order difference transform. At each iteration, $b^{(k)}$ is truncated by the soft thresholding function, and $B^{\mathrm{T}} b^{(k)}$ is considered as the noise in the image domain. In Eq (8), we choose the preconditioning matrix $S$ as the diagonal matrix $S^{(k)} := \mathrm{diag}(f^{(k)}/A^{\mathrm{T}}\mathbf{1})$ at the $k$th iteration. The operator $P_+$ is a projection onto the first octant. Specifically, for $x \in \mathbb{R}^d$, we have $\left(P_+(x)\right)_i = \max\{x_i, 0\}$. Motivated by [41], TV-PAPA calculates the components of vector $y := \mathrm{prox}_{(\lambda/\mu)\varphi}$ via the following formula:

$$[y_i, y_{d+i}, y_{2d+i}]^{\mathrm{T}} = \max\left\{\|[z_i, z_{d+i}, z_{2d+i}]^{\mathrm{T}}\| - \frac{\lambda}{\mu}, 0\right\} \frac{[z_i, z_{d+i}, z_{2d+i}]^{\mathrm{T}}}{\|[z_i, z_{d+i}, z_{2d+i}]^{\mathrm{T}}\|}, i = 1,2, \ldots, d. \tag{9}$$

Note that the iterative scheme of PAPA exhibits fast convergence due to the preconditioning technique and provides robust reconstruction. In addition, we compared the proposed CGAN-CDR with the MBIR method TV-PAPA. In order to evaluate the sinogram restoration performance of CGAN-CDR and its impact on reconstruction, we maintain the same solver for all competing methods.

## 3. Experimental design and results

First, we describe the datasets, evaluation metrics and experiment setting. Then, we compare CGAN-CDR with some state-of-the-art SPECT reconstruction methods and analyze the results from various aspects. We implement CGAN-CDR using PyTorch and the Python language. All experiments are performed on a GeForce RTX 3090.

### *3.1. Datasets*

The training and test datasets exploited in the numerical experiment are obtained using SIMIND [42,43], which is a nuclear medicine imaging simulation software based on Monte Carlo algorithm and can simulate a real gamma camera to image various phantoms. To generate datasets with high-quality references, three digital phantoms are simulated using SIMIND: an anatomical whole-body (WB) model from XCAT library, an anatomical torso model for ECT bone imaging (ECT) and a

digital geometric phantom consisting of activity gradients and uniform cylinders (geometric). In particular, we simulate a SIEMENS E.CAM gamma camera with low energy high resolution (LEHR) parallel-beam collimator. The detector orbit is circular, covering 360°, and the radius of rotation is set to 15 cm. The parallel-collimated SPECT projection data for the current simulation study consists of 120 projection views in a 128-dimensional detector array with detector element size 2.2 mm. We use an 18% main energy window centered at 141 keV. The gamma photons within this energy window are considered as primary or first-order scattered photons. Moreover, we simulate a scale of $10^9$ photon histories per projection view for each phantom to suppress the photon-flux fluctuation, obtaining the normal-dose projection dataset. The total numbers of photon counts detected in 120 projection views for the normal-dose projection data of three digital phantoms are presented in Table 1. The projection data at coronal and sagittal view angles for the three phantoms are further shown in Figure 5.

A total of 640 2D sinograms with clear data distribution are extracted from the projection data of the above three phantoms to generate the training and test datasets. Indeed, the training set consists of 512 sinograms, accounting for 80% of the total dataset, while the test set consists of 128 sinograms, accounting for 20% of the total dataset. The training and test datasets are split at the slice level. In fact, it is noticed that the neighborhood slices belonging to the same phantom still exhibit noticeable disparity. Based on this observation, we find that the training and test datasets split at slice level (it is guaranteed that the same slice does not appear in both datasets) still exhibit different data distributions to a certain extent, which could prevent information leakage to some extent. From Figure 6, it can be seen that there are obvious distribution differences between two sample neighborhood slices, especially the contrast along the bone structure. Statistically, a t-test uses t-distribution theory to infer the probability of a difference occurring, thus determining whether the difference between two samples is significant. The resultant p-value can be used to reflect the level of significant difference between the selected two samples. Therefore, we conducted a t-test between these two reconstructed slices and set a significance level of $p < 0.01$. As a result, the t-test demonstrated a significant difference between the underlying two neighborhood slices ($t = -4.323$, $p = 0.000016$).

The details of the datasets are also summarized in Table 1. The performance of the proposed neural network architecture at two levels of photon counting rates is explored. The two sets of low-count-rate sinograms are obtained via simulating scales of $10^7$ and $2 \times 10^7$ photon histories per projection view, which correspond to 1/100 and 1/50 of the normal-dose photon histories, respectively. The normal-dose sinograms (with $10^9$ photon histories per projection view) are regarded as label sinograms, and the mapping from low-count-rate sinograms to normal-dose sinograms is learned by the proposed network architecture. Note that the total number of photon histories represents the number of photons actually simulated in a SPECT simulation study. More photon histories indicate a higher dosage simulated and result in a lower degree of statistical uncertainty. The examples of a low-count-rate sinogram and its corresponding normal-dose sinogram are shown in Figure 7. The images reconstructed from the normal-dose sinograms by the TV-PAPA method with optimal regularization parameter are regarded as reference images for the training of the image-domain learning method. For fair comparison, we implemented 5-fold cross-validation without duplication for all the competing learning-based methods.

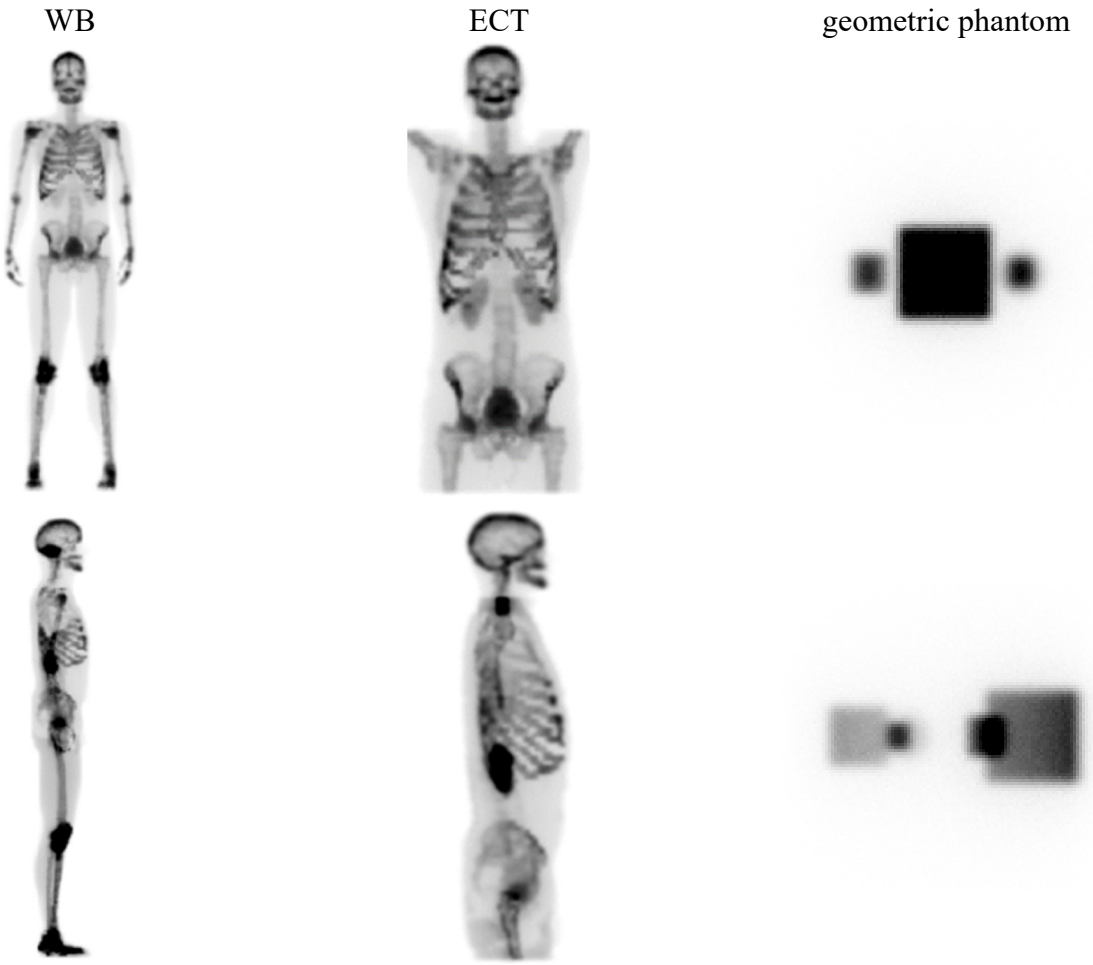


**Figure 5.** The projection data at coronal (top row) and sagittal (bottom row) view angles for WB, ECT and geometric phantoms, respectively.

(a) (b)

**Figure 6.** Two neighborhood slices extracted from the normal-dose reconstructed image for disparity comparison.

**Table 1.** Details of datasets. The total numbers of photon counts detected in 120 views for the normal-dose projection data are presented. The training and test datasets are split at the slice level.

| Phantom | The size of 3D projection data | The total number of detected photon counts | The number of sinograms in training set | The number of sinograms in test set |
|---|---|---|---|---|
| WB | 128 × 289 × 120 | $4.3 \times 10^7$ | 231 | 58 |
| ECT | 128 × 318 × 120 | $1.3 \times 10^8$ | 254 | 64 |
| geometric | 128 × 33 × 120 | $2.1 \times 10^7$ | 27 | 6 |

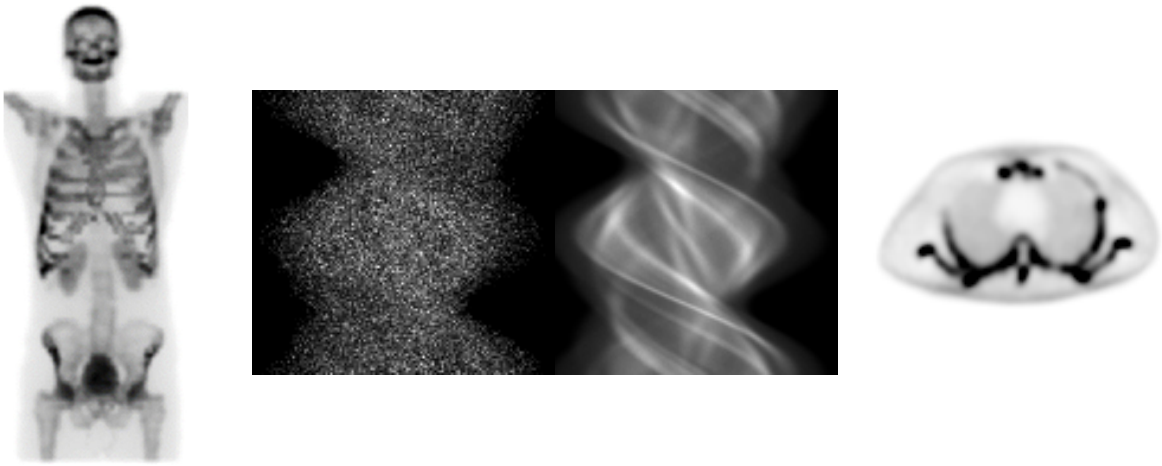

(a) (b) (c) (d)

**Figure 7.** Various forms of the projection data. (a) the projection at coronal view for ECT phantom; (b) a 2D sinogram extracted from the low-count-rate projection data of ECT phantom; (c) the 2D sinogram corresponding to subfigure (b), extracted from the normal-dose projection data of ECT phantom; (d) the reconstructed image of the normal-dose sinogram in subfigure (c) by TV-PAPA with regularization parameter of 0.01.

### *3.2. Evaluation metrics*

In order to carry out quantitative analysis, we use two global image quality metrics, the peak-to-noise ratio (PSNR) and structural similarity (SSIM), and two local image quality metrics, coefficient of variation (COV) and mean lesion contrast, to measure the quality of reconstructed images.

#### 3.2.1. Global image quality metrics

PSNR is an objective evaluation metric to measure the noise level or image distortion. The higher the PSNR is, the less distortion and the better quality of the generated image. It is defined as follows:

$$\mathrm{PSNR} = 10\log_{10}\left(\frac{\mathrm{MAX}_y^{\,2}}{\mathrm{MSE}}\right), \tag{10}$$

where $\mathrm{MSE}$ is the mean square error between reconstructed image and ground-truth, $y$ is the ground

truth, and $\mathrm{MAX}_y$ is the possible maximum pixel value in the image.

SSIM is a common similarity measure between two images. SSIM ranges from 0 to 1. The closer the value is to 1, the more similar two images are. The SSIM is a more suitable assessment of clinical information in medical images. It is defined as follows:

$$\mathrm{SSIM}(x,y)=\frac{(2\mu_x\mu_y+c_1)(2\sigma_{xy}+c_2)}{(\mu_x^2+\mu_y^2+c_1)(\sigma_x^2+\sigma_y^2+c_2)}, \tag{11}$$

where $x$ and $y$ are reconstructed image and ground truth, respectively, $\mu_x$ is the mean of $x$, $\mu_y$ is the mean of $y$, $\sigma_x^2$ and $\sigma_y^2$ represent the variances of $x$ and $y$, respectively, $\sigma_{xy}$ is the covariance of $x$ and $y$, and $c_1$, $c_2$ are two variables to stabilize the division with weak denominator.

3.2.2. Local image quality metrics

For better quantitative analysis, we further exploit local image quality metrics, coefficient of variation (COV) and mean lesion contrast, to evaluate the reconstructed images. In an image processing task, COV is usually employed to characterize the pixel-level variability in the restored image, and it is defined as follows:

$$\mathrm{COV}_k \coloneqq \frac{\mathrm{Std}_k}{m_k}, \tag{12}$$

where $\mathrm{Std}_k$ denotes the standard deviation of the $k$th region-of-interest (ROI), and $m_k$ denotes the mean value of the $k$th ROI.

The mean lesion contrast provides a useful measure for the contrast recovery degree of the selected ROI quantitatively. We calculate the mean lesion contrast using 2D ROIs in the transaxial cross-sections through sphere center. The background ROIs are of the same size as the target. We define 5 of them distributed around the corresponding target and obtain their mean value. The absolute mean contrast is then defined as follows:

$$C_a \coloneqq \langle |T-B| \rangle, \tag{13}$$

where $T$ is the mean activity in the target ROI for a given noise realization, $B$ is the mean activity over 5 surrounding circular background ROIs for the same realization, and the notation $\langle\cdot\rangle$ denotes the average over multiple independent noise realizations.

*3.3. Experimental setting*

The loss weights in the minimax optimization model (3) are determined as $\omega = 0.6$ and $\lambda = 0.01$. The underlying minimax optimization problem is solved by ADAM algorithm in an alternating fashion with $\beta_1$ = 0.5 and $\beta_2$ = 0.999. The maximum number of training epochs is 1000. The learning rate is set to $2\times10^{-4}$ for the first 900 epochs. In the remaining 100 epochs, the learning rate gradually decreases from $2\times10^{-4}$ to zero for a stabilized convergence.

In this work, we compare the proposed CGAN-CDR with the traditional MBIR method TV-PAPA, a sinogram-domain learning method with U-Net, and two image-domain restoration methods, block-matching and 3D filtering (BM3D) and an image-domain learning method with residual coder

convolutional neural network (RED-CNN).

TV-PAPA was proposed to solve the penalized maximum likelihood emission computed tomography (ECT) reconstruction problem [6]. More details of TV-PAPA are given in Section 2.3. In the numerical experiment, we observe that reconstruction of the low-count-rate projection data for ECT phantom achieves the optimal visual effect when the regularization parameter of TV-PAPA is set to 1.2. For the WB and digital geometric phantoms, the optimal visual effects of low-count-rate reconstruction are obtained with regularization parameters of 0.2 and 0.15, respectively. The competing U-Net shares the same architecture as the generator network $G$ in CGAN-CDR. BM3D [44] is recognized as a classical image denoising algorithm. We use a maximum likelihood expectation maximization (ML-EM) algorithm to reconstruct low-count-rate sinograms and then employ BM3D to denoise the reconstructed images. RED-CNN [18] is a well-known image-domain learning method for restoring high-quality reconstructed images

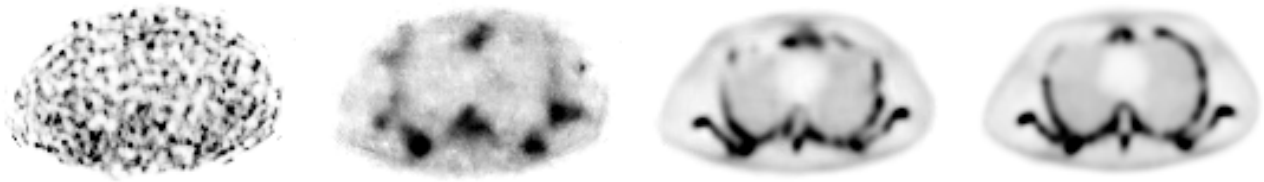

(a) (b) (c) (d)

**Figure 8.** Reconstructed images of low-count-rate test sinogram: (a) raw low-count-rate reconstructed image as input of RED-CNN, (b) the reconstructed image of original RED-CNN network structure, (c) the reconstructed image of modified RED-CNN and (d) reconstructed image of normal-dose sinogram as the label image.

In order to achieve better performance for RED-CNN, we have modified the original network structure of RED-CNN to fit the underlying training dataset. While maintaining the residual structure, five convolution and deconvolution modules in the original network architecture are extended to eleven modules, and the number of convolution kernels is increased from 96 to 128. Moreover, the activation function for the encoding modules is changed from the original ReLU to LeakyReLU. The above modifications can enlarge the receptive field of RED-CNN and better capture and characterize the more distant correlations (for example, the bone structure) in reconstructed images. The visual improvement of the modified RED-CNN is shown in Figure 8. We can readily see that the modified RED-CNN has better restoration performance, and the restored image exhibits more reasonable visual appearance.

### *3.4. Visual comparison*

In order to make a comprehensive visual comparison among the competing restoration and reconstruction methods, we show and qualitatively evaluate the restored sinograms, when available, and reconstructed images in this section. In both sinogram- and image-domain methods, the goal is always to reconstruct high-quality images from low-dose SPECT projection data.

### 3.4.1. Visual comparison of restored sinograms

Regarding projection-domain performance, we can see from Figure 9 that both U-Net and CGAN-CDR exhibit reasonable sinogram restoration. When compared with the normal-dose sinogram, the restored sinogram by CGAN-CDR is more realistic-looking than that produced by U-Net, both in sinusoidal detail and contrast. Indeed, we readily find more details and better contrast of the restored sinogram by CGAN-CDR shown in Figure 10, which demonstrates the zoomed-in yellow ROI in Figure 9. As indicated by the blue and red arrows, the proposed CGAN-CDR can better restore the original sinusoidal waves and recover contrast of the normal-dose sinogram, as compared to U-Net. This sinogram realism gain may lead to an improvement of global reconstruction accuracy and structure restoration in the image domain, which shall be explored in subsequent sections.

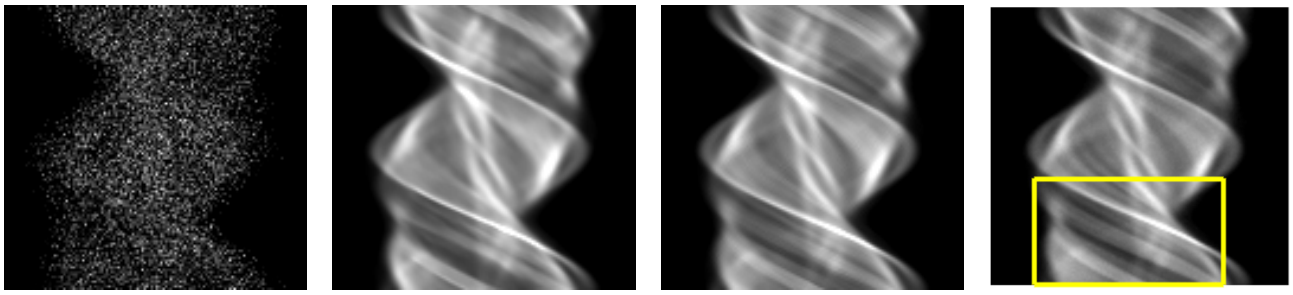

(a) (b) (c) (d)

**Figure 9.** The restored sinograms by two competing projection-domain models: (a) low-dose sinogram, (b) U-Net restoration, (c) CGAN-CDR restoration and (d) normal-dose sinogram.

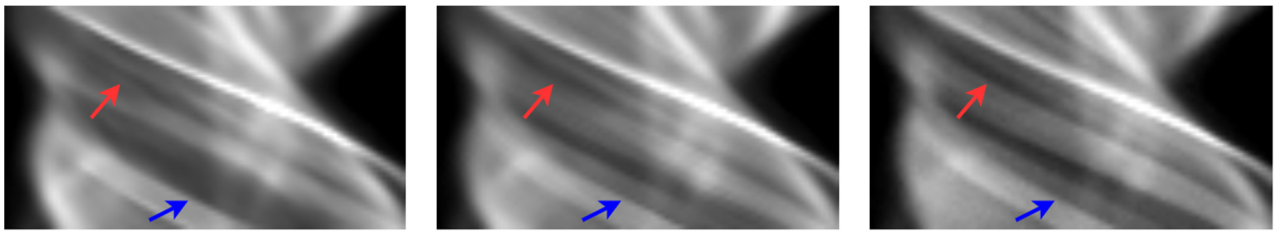

(a) (b) (c)

**Figure 10.** Zoomed-in images of the yellow ROI in Figure 9: (a) U-Net, (b) CGAN-CDR and (c) normal-dose sinogram.

### 3.4.2. Visual comparison of reconstructed images

In order to evaluate the subsequent reconstruction performance of the proposed sinogram restoration model, we select a representative slice from the ECT phantom for visual comparison, as shown in Figure 11. For all the competing sinogram-domain restoration methods and the image-domain RED-CNN, we reconstruct the restored/low-count-rate sinograms using TV-PAPA with a regularization parameter of 0.01. When TV-PAPA is used as a competing reconstruction method, we determine its optimal regularization parameter for the respective phantom, as indicated in Section 3.3.

For the image-domain denoising algorithm BM3D, we employ an ML-EM algorithm to reconstruct the low-count-rate sinograms. We have marked three ROIs in Figure 11(g) for highlighted visual assessment.

It is obvious that in the case of low-count-rate sinogram reconstruction, the traditional handcrafted methods BM3D and TV-PAPA exhibit much worse reconstruction visual appearance, as compared to the learning-based approaches. The severe noise and the loss of anatomical structures in the reconstructed images may limit the clinical use of handcrafted methods in very-low-dose SPECT imaging. Moreover, in ROI II, both CGAN-based sinogram restoration methods can better recover the accurate bone structure, while the image-domain RED-CNN and the projection-domain U-Net perform inferiorly and exhibit structural deformation to different extents. In ROIs I and III, we further see that RED-CNN still exhibits moderate oscillation and severe structural deformation. U-Net and CGAN-based sinogram restoration methods, on the contrary, maintain the original structural characteristics of the label image. In addition, as compared to the CGAN-based projection-domain methods, the U-Net sinogram restoration method tends to produce blurrier bone structures and higher noise. Among all the above competing methods, CGAN-CDR performs the best in terms of noise and artifact suppression, contrast recovery and structure preservation. In particular, CGAN-CDR exhibits the best denoising and contrast-enhancement performance in the low-contrast region (i.e., the chest region).

In sum, Figure 11 shows that the proposed CGAN-CDR facilitates the generation of a realistic looking image compared to the label. For reference, we indicate the PSNR (the first value in the bracket) and SSIM (the second value in the bracket) metrics of the six competing methods obtained at the underlying cross section in the caption of Figure 11.

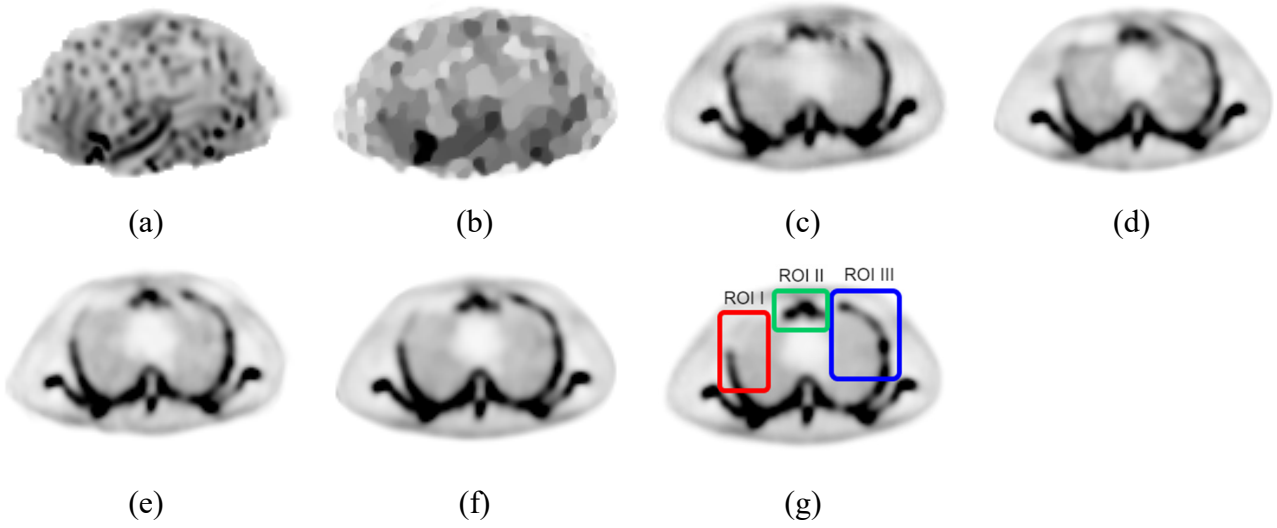


**Figure 11.** Transaxial cross sections through chest regions, generated using (a) BM3D (23.25, 0.6960), (b) TV-PAPA (23.49, 0.7472), (c) RED-CNN (28.97, 0.9187), (d) U-Net (33.13, 0.9579), (e) CGAN (36.66, 0.9746), and (f) CGAN-CDR (36.43, 0.9810), and the corresponding (g) label image.

For a closer look at the visual comparison, the image patches in ROI III for the four learning-based restoration methods in Figure 11 are zoomed in, as shown in Figure 12. From a visual perspective, the bone structures restored by the image-domain RED-CNN exhibit blurry appearance and misleading contrast, and they suffer from severe deformation. The projection-domain U-Net performs relatively

poorly in both contrast recovery along the bone structure and noise suppression. In contrast with the above network architectures, which typically exploit component-wise loss functions to compare the network output against the label at pixel or detector-bin level, the CGAN-based projection-domain methods exhibit obvious advantage in structure maintenance and contrast recovery, as pointed to by red arrows in Figure 12. The proposed CGAN-CDR performs the best in every visual aspect, especially in noise reduction, contrast recovery and structural detail preservation. Overall, CGAN-CDR generates the most realistic-looking sinogram and reconstructed image among competing methods.

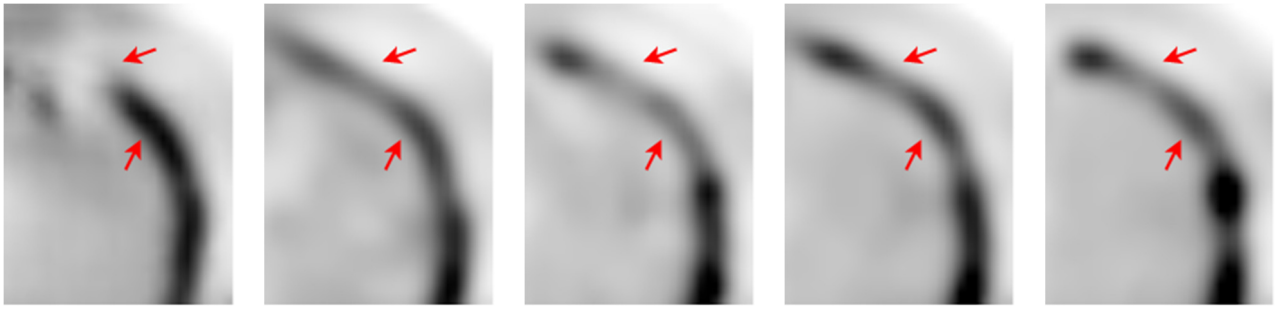

(a) (b) (c) (d) (e)

**Figure 12.** Zoomed-in area in blue box in Figure 11. (a) RED-CNN, (b) U-Net, (c) CGAN, (d) CGAN-CDR, (e) label.

To further compare the proposed CGAN-CDR with the image-domain RED-CNN and the projection-domain U-Net in the reconstruction of the geometric phantom, we select the central cross-sectional slice from the geometric phantom for presentation. We can see from Figure 13 that learning-based methods can well maintain the original geometric structures in the geometric phantom. The image-domain RED-CNN realizes high-contrast yet high-oscillation image restoration. In terms of noise suppression, RED-CNN and U-Net perform relatively poorly, as indicated in the rectangular regions. The proposed CGAN-CDR performs the best in both contrast recovery and noise suppression, without loss of spatial resolution. As shown in Figure 13(d), the ROIs in the yellow rectangle and four red circles are used for calculation of coefficient of variation and mean lesion contrast, respectively, in the subsequent Section 3.6.2.

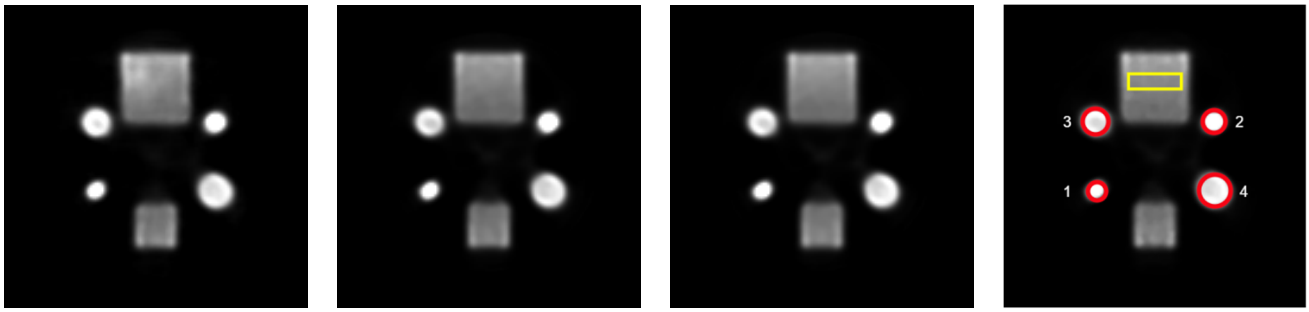


(a) (b) (c) (d)

**Figure 13.** Reconstructed cross-sectional slices of geometric phantom. The areas in yellow rectangle and four red circles indicate ROIs for calculation of image quality metrics. (a) RED-CNN, (b) U-Net, (c) CGAN-CDR, and (d) label reconstruction.

To distinguish the visual performance of the competing methods more intuitively, we also present surface plots and corresponding contours for better visualization in Figure 14. In terms of contour plots, both the proposed CGAN-CDR and the projection-domain U-Net outperform the image-domain RED-CNN in the sense that the former two methods can better preserve the linearly varying contours along the horizontal direction and avoid closed contours that indicate local oscillations. Furthermore, in the low-activity region (as indicated by the cold contours), the CGAN-CDR model achieves superior performance in preserving parallel contour lines, as compared to the U-Net model. This indicates that in the cold region of an image, the proposed CGAN-CDR may have better noise suppression ability than U-Net.

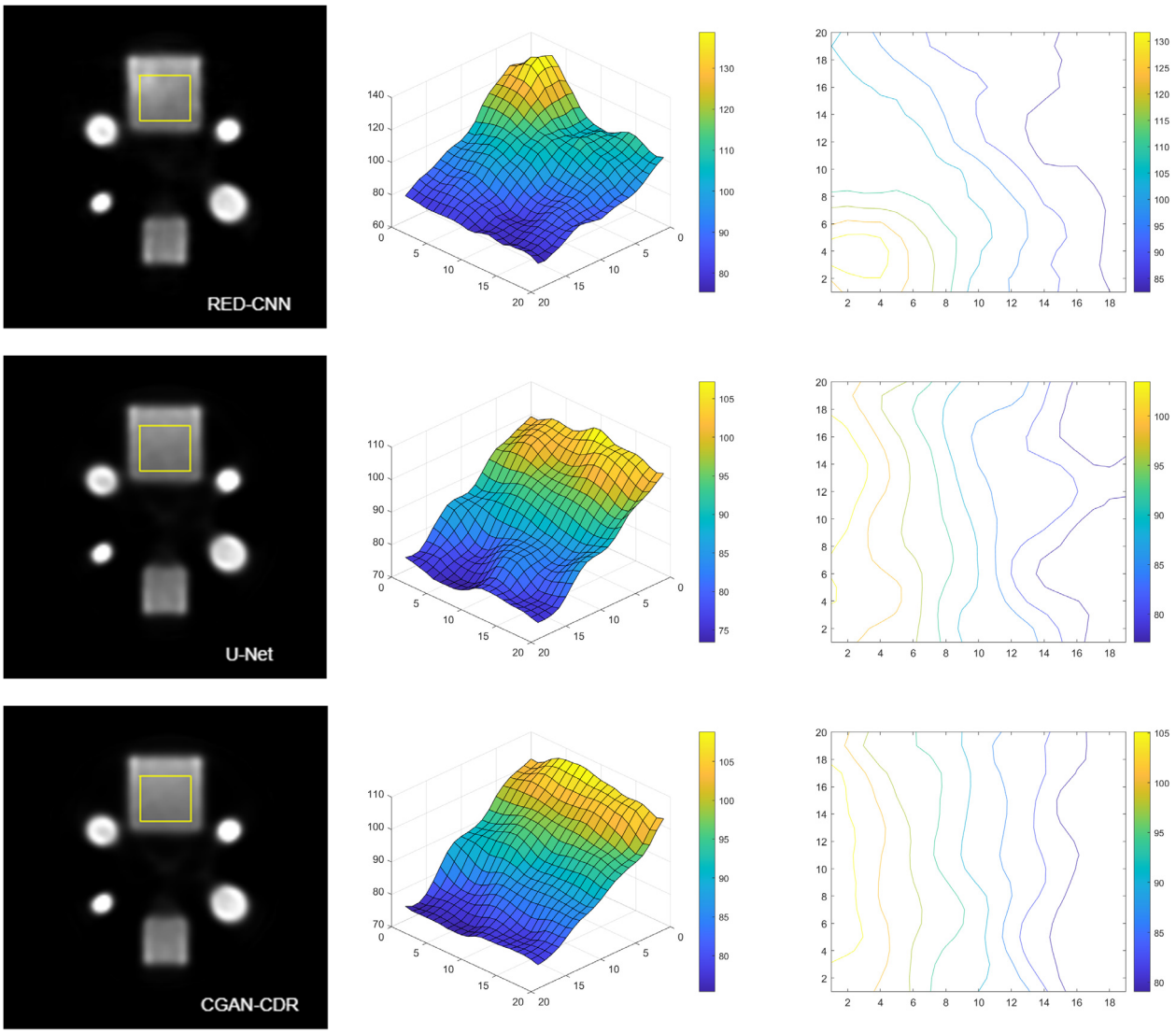


**Figure 14.** Surface plots and corresponding contour lines of reconstructed geometric cross-sectional slices by three learning-based methods.

### *3.5. Quantitative results*

#### 3.5.1. Global image quality analysis

The global image quality metrics PSNR and SSIM of reconstructed images are employed for quantitative comparison of reconstruction accuracy. Mean values of PSNR and SSIM averaged over the test dataset of WB and ECT phantoms are shown in Table 2. Traditional handcrafted methods BM3D and TV-PAPA produce much lower PSNR and SSIM values, as compared to learning-based approaches. It is indicated that in very-low-dose SPECT imaging, handcrafted methods perform rather poorly in overall reconstruction accuracy. Moreover, the proposed CGAN-CDR obtains the highest average values in both PSNR and SSIM. It is notable that the above quantitative results of reconstruction accuracy are essentially in agreement with the visual performance in Figure 11. This quantitative experiment suggests that CGAN-CDR can maintain high-accuracy image reconstruction in a low-dose SPECT imaging scenario. The overall accuracy improvement comes primarily from the introduction of an adversarial network into the traditional optimization process. The cross-domain regularization can further improve reconstruction accuracy and better suppress noise and recover image contrast (as shown in the subsequent section), via imposing similarity penalty in both sinogram and image domains.

**Table 2.** Quantitative results of global reconstruction accuracy of ECT phantoms with six competing reconstruction/restoration methods.

| Method | PSNR | SSIM |
|---|---|---|
| BM3D | 22.88 | 0.7315 |
| TV-PAPA | 24.79 | 0.8234 |
| RED-CNN | 31.54 | 0.9518 |
| U-Net | 36.17 | 0.9753 |
| CGAN | 37.68 | 0.9763 |
| CGAN-CDR | **38.75** | **0.9855** |

#### 3.5.2. Local image quality analysis

In order to better assess the local quantitative performance of the proposed CGAN-CDR and compare with the other two learning-based methods, RED-CNN and U-Net, two sets of ROIs in the digital geometric phantom are selected to calculate two local image quality metrics, coefficient of variation (COV) and mean lesion contrast, respectively.

**Table 3.** Quantitative comparison of COV for four competing methods obtained at the yellow rectangular ROI in Figure 13(d).

| Method | Coefficient of variation |
|---|---|
| RED-CNN | 0.0996 |
| U-Net | 0.0360 |
| CGAN | 0.0337 |
| CGAN-CDR | **0.0312** |

The yellow rectangular ROI in Figure 13(d) was selected for COV calculation. Indeed, the amplitude of COV can be used to represent the degree of noise suppression. Numerical comparison of COV is shown in Table 3. We can see that the proposed CGAN-CDR achieves the lowest COV value for the selected flat, wide ROI in the low-dose imaging scenario. In particular, as compared to the pure CGAN, the proposed CGAN-CDR exhibits slightly better COV performance. This observation validates the feasibility of cross-domain regularization in terms of noise suppression.

As shown in Figure 13(d), four red circular ROIs were further selected for calculation of mean lesion contrast. We particularly select three central slices from the geometric phantom and exploit ROIs with the above location and size at each slice. We then calculate the average of mean lesion contrasts over three slices for each underlying circular ROI. Figure 15 shows the comparison of three competing methods in the metric of mean lesion contrast. The horizontal labels 1 to 4 represent, respectively, four circular ROIs with different radii from small to large. We note that the projection-domain CGAN-CDR and U-Net both perform better than the image-domain RED-CNN in contrast recovery, especially on small ROIs (e.g., ROIs 1 and 2). Contrast increases monotonically with the radius of ROI. Small ROI can be employed to simulate early lesion. Hence, contrast recovery of small ROI plays an important role in the SPECT reconstruction task. Figure 15, together with the above image quality analysis, suggests that the proposed method generates reconstructed images of superior quality, both qualitatively and quantitatively, without sacrificing the image contrast.

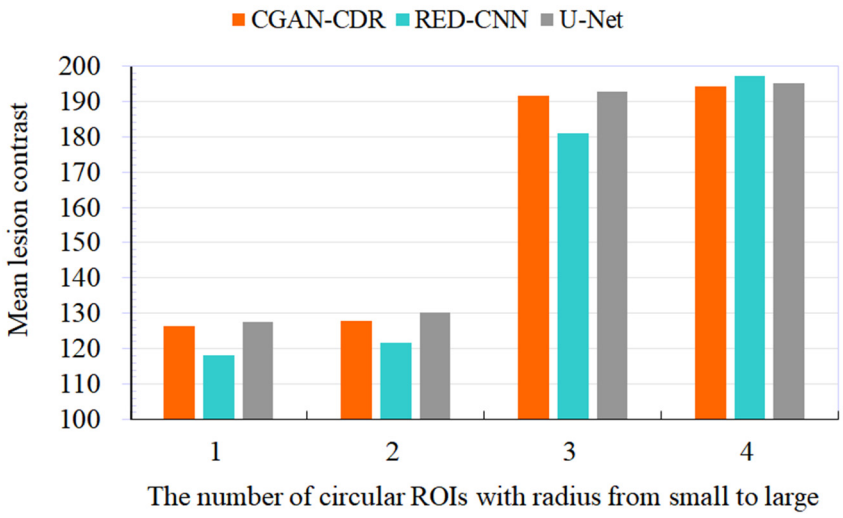


**Figure 15.** Averaged mean lesion contrasts for four circular ROIs in the geometric phantom.

### *3.6. Performance robustness*

In order to verify the robustness of the proposed CGAN-CDR model with respect to different noise levels, we further simulated a higher noise level for a representative sinogram selected from the test dataset. Indeed, we generated Poisson-distributed projection data for a transaxial slice crossing through the chest region and lying in the test dataset via a random number generator. The generated sinogram exhibits higher-level Poisson noise, as compared to the SIMIND-simulated training set of projection data (shown in Figure 16).

Three competing models, RED-CNN, U-Net and the proposed CGAN-CDR, learned from the

aforementioned training dataset and were employed to restore the underlying higher-noise test sinogram, as shown in Figure 17. Note that RED-CNN is a post-learning method applied in the image domain, while U-Net and the proposed CGAN-CDR are pre-learning methods performing sinogram denoising. From Figure 17, we see that in a transferred scenario of higher noise level, the proposed CGAN-CDR can better recover the bone structure of the reconstructed image, especially the detailed structure around the spine. This observation demonstrates the robustness of CGAN-CDR in structural maintenance with respect to different noise levels.

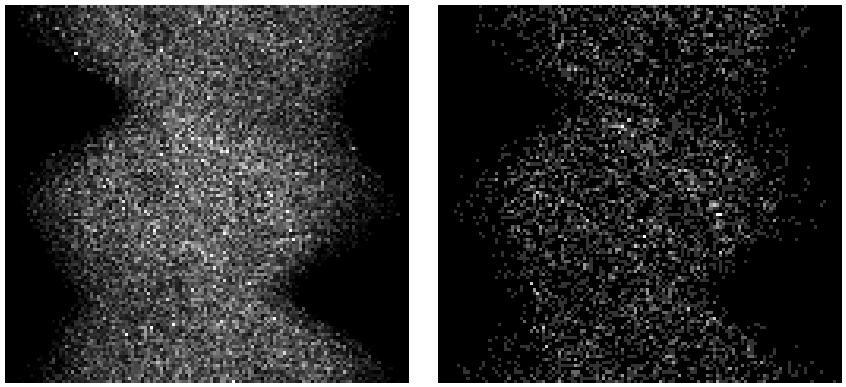

(a) (b)

**Figure 16.** Poisson noise contaminated sinogram for a transaxial slice crossing through the chest region and lying in the test dataset: (a) SIMIND-simulated sinogram for the underlying test slice; (b) higher-noise sinogram created by a random number generator.

(a) (b) (c) (d)

**Figure 17.** Reconstructed images of the underlying test slice restored by three competing models: (a) the image-domain RED-CNN, (b) the projection-domain U-Net, (c) the proposed projection-domain CGAN-CDR and (d) label reconstruction.

### *3.7. Test results of different phantom*

To explore the generalizability performance of the proposed CGAN-CDR, an adult male phantom (XCAT-male) was introduced from the XCAT library with different data distribution from the training data. We utilize SIMIND to simulate a SIEMENS E.CAM gamma camera with low energy high resolution (LEHR) parallel-beam collimator. The detector orbit is circular, covering 360°, and the radius of rotation is set to 15 cm. The parallel-collimated SPECT projection data for the current simulation study consists of 120 projection views in a 128-dimensional detector array with detector

element size 2.2 mm. We use an 18% main energy window centered at 141 keV. The low-count-rate projection data is obtained via simulating a scale of $10^4$ photon histories per projection view. A total of 206 sinograms of valid test data are obtained from the XCAT-male phantom. A representative reconstructed slice in the chest region of the XCAT-male phantom under the normal-dose acquisition is shown in Figure 18, and its bone structure is different from the samples in Section 3.1. The training data in Section 3.1 is used to perform the respective training for all comparison methods, and then the data of the XCAT-male phantom is tested. Similarly, we evaluate the reconstruction accuracy of each method for test data with different data distribution by calculating average PSNR and SSIM, and the results are shown in Table 4. This simulation shows that for the XCAT-male phantom with different data distribution from the training data, the learning-based methods outperform the traditional iterative method TV-PAPA in terms of reconstruction accuracy. The proposed CGAN-CDR exhibits potentially superior generalizability performance in terms of overall reconstruction accuracy, as compared to the other competing learning-based methods.

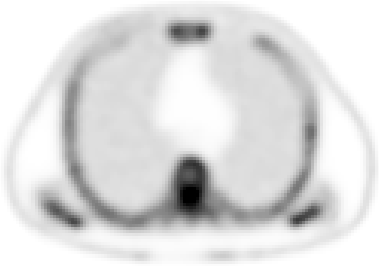

**Figure 18.** A representative reconstructed slice in the chest region of the XCAT-male phantom under the normal-dose acquisition.

**Table 4.** Quantitative results of global reconstruction accuracy of XCAT-male phantom with four competing reconstruction/restoration methods. The regularization parameter of TV-PAPA is 1.

| Method | PSNR | SSIM |
|---|---|---|
| TV-PAPA | 20.90 | 0.6858 |
| U-Net | 22.92 | **0.7477** |
| CGAN | 22.16 | 0.6982 |
| CGAN-CDR | **23.44** | 0.7435 |

## 4. Discussion

In SPECT imaging, the dose of radioactive tracer is a crucial factor for image quality; however, the ionizing radiation induced by the radiotracer poses a potential hazard to human health. Therefore, reducing the dose of the radiotracer meanwhile guaranteeing the image quality is a critical issue in the research of SPECT imaging. In the acquisition mode of reduced photon counts, the projection data exhibits increased Poisson noise, more-distant correlation and lower contrast. Such data degradations may be further amplified in the image domain due to the ill-posedness of the reconstruction problem, which intrinsically restricts reconstruction algorithms to obtain high-quality results. To address these

challenges, we propose the network model CGAN-CDR for low-count-rate SPECT sinogram restoration. The adversarial loss can facilitate the recovery of detailed sinusoidal features and contrast in the projection sinogram. In order to further guarantee high accuracy and low noise of the generated sinogram, we add a cross-domain regularization function to the adversarial loss, which can address the issue of ill-posedness due to image reconstruction. The numerical simulation results indicate that the proposed model is superior to the other competing models in terms of both visual appearance and quantitative analysis.

The generator of the proposed CGAN-CDR model is composed of an encoder and a decoder. The encoder model stepwise extracts multiscale sinusoidal features from the input sinogram, and the decoder model stepwise rebuilds the feature representation into a sinogram. We particularly introduce long skip connections into the network architecture of the generator via concatenation in a symmetrical manner, so that the low-level features in the projection domain (i.e., the contrast and contours of sinusoidal waves) can be better shared and reused, and the spatial and angular sinogram information lost during down-sampling can be better recovered. We employ the discriminator in the previous PatchGAN network model to capture and characterize the detailed sinusoidal features within sinogram patches, since various local patches in a sinogram exhibit different spatial variations and correlations, and thus should be evaluated independently. The realistic prediction achieved by an evaluation matrix, instead of by a single evaluation value per traditional GAN, can effectively characterize detailed features in local receptive fields. Numerical results show that the proposed network model exhibits good performance in the task of low-count-rate sinogram restoration.

The projection-domain pre-learning method, by its essence, cannot satisfactorily address the issue of ill-posedness due to image reconstruction. Provided that the training data are sufficiently abundant, a better approach for the above issue is to perform network learning in both projection and image domains via combining the recently developed dual-domain strategy with adversarial framework. The projection-domain consistency constraint directly constrains the generator via penalizing the difference between the generator output and the label sinogram in a component-wise sense, which helps recover accurate contrast between sinusoidal waves in the sinogram restoration process. The image-domain consistency regularization imposes a similarity constraint on the reconstructed images of the generated and label sinograms, which can address the issue of ill-posedness and serves as an indirect constraint on the generator. Therefore, an effective noise-suppressed and artifact-reduced image-domain regularization can in turn enhance the quality of generated sinograms. Moreover, since the training procedure of an adversarial framework is rather time-consuming, how to develop a lightweight adversarial network remains a challenging future research direction.

## 5. Conclusions

In this paper, the CGAN-CDR model based on a generative adversarial network is proposed for low-dose sinogram restoration to suppress random oscillation and enhance contrast in SPECT imaging. The adversarial framework in CGAN-CDR can better restore the detailed global sinusoidal features and recover the original contrast of the normal-dose sinogram. Meanwhile, the cross-domain optimization in both projection and image domains can effectively ameliorate the issue of ill-posedness and serve as both direct and indirect constraint on the generator; thereby, it helps to achieve excellent performance in noise reduction and contrast recovery. Extensive numerical experiments show that learning-based methods are superior to traditional methods. Moreover, the proposed CGAN-CDR

performs best both qualitatively and quantitatively, indicating that the proposed model has the potential to reduce the radioactive tracer dose required for SPECT imaging without compromising the quality of reconstructed images.

**Acknowledgments**

This work is supported in part by the Natural Science Foundation of China under grant 11771464, by the Natural Science Foundation of Guangdong Province under grants 2022A1515012379 and 2021A1515012290, by the Opening Project of Guangdong Province Key Laboratory of Computational Science at Sun Yat-sen University under grant 2021007, by the Science and Technology Program of Guangzhou under grant 201804020053, by Guangdong Provincial Key Laboratory of Cyber-Physical Systems under grant 2020B1212060069 and by National & Local Joint Engineering Research Center of Intelligent Manufacturing Cyber-Physical Systems.

**Conflict of interest**

The authors have no relevant financial or non-financial interests to disclose.

**References**

1. H. A. Ziessman, J. P. O'Malley, J. H. Thrall, *Nuclear Medicine: The Requisites*, Elsevier, 2014.
2. P. Ritt, H. Vija, J. Hornegger, T. Kuwert, Absolute quantification in SPECT, *Eur. J. Nucl. Med. Mol. Imaging*, **38** (2011), 69–77. https://doi.org/10.1007/s00259-011-1770-8
3. X. Niu, Y. Yang, M. Jin, M. N. Wernick, M. A. King, Effects of motion, attenuation, and scatter corrections on gated cardiac SPECT reconstruction, *Med. Phys.*, **38** (2011), 6571–6584. https://doi.org/10.1118/1.3660328
4. R. G. Wells, Dose reduction is good but it is image quality that matters, *J. Nucl. Cardiol.*, **1** (2018), 1–3. https://doi.org/10.1007/s12350-018-1378-5
5. J. Zhang, S. Li, A. Krol, C. R. Schmidtlein, E. Lipson, D. Feiglin, et al., Infimal convolution-based regularization for SPECT reconstruction, *Med. Phys.*, **45** (2018), 5397–5410. https://doi.org/10.1002/mp.13226
6. A. Krol, S. Li, L. Shen, Y. Xu, Preconditioned alternating projection algorithms for maximum a posteriori ECT reconstruction, *Inverse Probl.*, **28** (2012), 115005. https://doi.org/10.1088/0266-5611/28/11/115005
7. Y. Luo, M. Wei, S. Li, J. Ling, G. Xie, S. Yao, An effective co-support guided analysis model for multi-contrast MRI reconstruction, *IEEE J. Biomed. Health*, (2023). https://doi.org/10.1109/JBHI.2023.3244669
8. H. Zhang, B. Dong, A review on deep learning in medical image reconstruction, *J. Oper. Res. Soc. China*, **8** (2020), 311–340. https://doi.org/10.1007/s40305-019-00287-4
9. I. Häggström, C. R. Schmidtlein, G. Campanella, T. J. Fuchs, DeepPET: A deep encoder-decoder network for directly solving the PET reconstruction inverse problem, *Med. Image Anal.*, **54** (2019), 253–262. https://doi.org/10.1016/j.media.2019.03.013
10. B. Zhu, J. Z. Liu, S. F. Cauley, B. R. Rosen, M. S. Rosen, Image reconstruction by domain-transform manifold learning, *Nature*, **555** (2018), 487–492. https://doi.org/10.1038/nature25988

11. H. Zhang, B. Dong, B. Liu, JSR-Net: A deep network for Joint Spatial-Radon domain CT reconstruction from incomplete data, in *IEEE International Conference on Acoustics, Speech and Signal Processing (ICASSP)*, (2019), 3657–3661. https://doi.org/10.1109/ICASSP.2019.8682178
12. Y. Yang, H. Li, Z. Xu, J. Sun, Deep ADMM-Net for compressive sensing MRI, *Adv. Neural Inf. Process. Syst.*, **29** (2016), 10–18.
13. Y. Yang, H. Li, Z. Xu, ADMM-CSNet: A deep learning approach for image compressive sensing, *IEEE Trans. Pattern Anal. Mach. Intell.*, **42** (2018), 521–538. https://doi.org/10.1109/TPAMI.2018.2883941
14. J. Adler, O. Öktem, Learned primal-dual reconstruction, *IEEE Trans. Med. Imaging*, **37** (2018), 1322–1332. https://doi.org/10.1109/TMI.2018.2799231
15. B. Zhou, X. Chen, S. K. Zhou, J. S. Duncan, C. Liu. DuDoDR-Net: Dual-domain data consistent recurrent network for simultaneous sparse view and metal artifact reduction in computed tomography, *Med. Image Anal.*, **75** (2022), 102289. https://doi.org/10.1016/j.media.2021.102289
16. M. Li, W. Hsu, X. Xie, J. Cong, W. Gao. SACNN: Self-attention convolutional neural network for low-dose CT denoising with self-supervised perceptual loss network, *IEEE Trans. Med. Imaging,* **39** (2020), 2289–2301. https://doi.org/10.1109/TMI.2020.2968472
17. W. Bae, J. J. Yoo, J. C. Ye, Beyond deep residual learning for image restoration: persistent homology-guided manifold simplification, in *IEEE Conference on Computer Vision and Pattern Recognition (CVPR) Workshops*, (2017), 145–153. https://doi.org/10.1109/CVPRW.2017.152
18. H. Chen, Y. Zhang, M. K. Kalra, F. Lin, Y. Chen, P. Liao, et al., Low-dose CT with a residual encoder-decoder convolutional neural network, *IEEE Trans. Med. Imaging*, **36** (2017), 2524–2535. https://doi.org/10.1109/TMI.2017.2715284
19. Z. Zhang, X. Liang, X. Dong, Y. Xie, G. Cao, A sparse-view CT reconstruction method based on combination of DenseNet and deconvolution, *IEEE Trans. Med. Imaging*, **37** (2018), 1407–1417. https://doi.org/10.1109/TMI.2018.2823338
20. J. C. Ye, Y. Han, E. Cha, Deep convolutional framelets: A general deep learning framework for inverse problems, *SIAM J. Imaging Sci.*, **11** (2018), 991–1048. https://doi.org/10.1137/17M1141771
21. Y. Han, J. C. Ye, Framing U-Net via deep convolutional framelets: Application to sparse-view CT, *IEEE Trans. Med. Imaging*, **37** (2018), 1418–1429. https://doi.org/10.1109/TMI.2018.2823768
22. C. Szegedy, W. Liu, Y. Jia, P. Sermanet, S. Reed, D. Reed, et al., Going deeper with convolutions, in *IEEE Conference on Computer Vision and Pattern Recognition*, (2015), 1–9. https://doi.org/10.1109/CVPR.2015.7298594
23. S. Xie, X. Zheng, Y. Chen, L. Xie, J. liu, Y. Zhang, et al., Artifact removal using improved GoogLeNet for sparse-view CT reconstruction, *Sci. Rep.*, **8** (2018), 1–9. https://doi.org/10.1038/s41598-018-25153-w
24. H. Lee, J. Lee, H. Kim, B. Cho, S. Cho, Deep-neural-network-based sinogram synthesis for sparse-view CT image reconstruction, *IEEE Trans. Radiat. Plasma Med. Sci.*, **3** (2018), 109–119. https://doi.org/10.1109/TRPMS.2018.2867611
25. B. Pan, N. Qi, Q. Meng, J. Wang, S. Peng, C. Qi, et al., Ultra high speed SPECT bone imaging enabled by a deep learning enhancement method: A proof of concept, *EJNMMI Phys.*, **9** (2022), 1–15. https://doi.org/10.1186/s40658-022-00472-0

26. H. Yuan, J. Jia, Z. Zhu, Sipid: A deep learning framework for sinogram interpolation and image denoising in low-dose CT reconstruction, in *IEEE 15th International Symposium on Biomedical Imaging (ISBI)*, (2018), 1521–1524. https://doi.org/10.1109/ISBI.2018.8363862
27. X. Dong, S. Vekhande, G. Cao, Sinogram interpolation for sparse-view micro-CT with deep learning neural network, in *SPIE Medical Imaging 2019: Physics of Medical Imaging*, (2019), 109482O. https://doi.org/10.1117/12.2512979
28. C. Chrysostomou, L. Koutsantonis, C. Lemesios, C. N. Papanicolas, SPECT angle interpolation based on deep learning methodologies, in *IEEE Nuclear Science Symposium and Medical Imaging Conference (NSS/MIC)*, (2020), 1–4. https://doi.org/10.1109/NSS/MIC42677.2020.9507966
29. I. Shiri, P. Sheikhzadeh, M. R. Ay, Deep-fill: Deep learning based sinogram domain gap filling in positron emission tomography, preprint, arXiv: 1906.07168. https://doi.org/10.48550/arXiv.1906.07168
30. S. Li, W. Ye, F. Li, LU-Net: Combining LSTM and U-Net for sinogram synthesis in sparse-view SPECT reconstruction, *Math. Biosci. Eng.*, **19** (2022), 4320–4340. https://doi.org/10.3934/mbe.2022200
31. E. Xie, P. Ni, R. Zhang, X. Li. Limited-angle CT Reconstruction with generative adversarial network sinogram inpainting and unsupervised artifact removal, *Appl. Sci.*, **12** (2022), 6268. https://doi.org/10.3390/app12126268
32. I. Goodfellow, J. Pouget-Abadie, M. Mirza, B. Xu, D. Warde-Farley, S. Ozair, et al., Generative adversarial nets, *Commun. ACM*, **63** (2020), 139–144. https://doi.org/10.1145/3422622
33. C. Tang, W. Zhang, L. Wang, A. Cai, N. Liang, L. Li, et al., Generative adversarial network-based sinogram super-resolution for computed tomography imaging, *Phys. Med. Biol.*, **65** (2020), 235006. https://doi.org/10.1088/1361-6560/abc12f
34. Z. Li, W. Zhang, L. Wang, A. Cai, N. Liang, B. Yan, et al., A sinogram inpainting method based on generative adversarial network for limited-angle computed tomography, in *15th International Meeting on Fully Three-Dimensional Image Reconstruction in Radiology and Nuclear Medicine*, (2019), 345–349. https://doi.org/10.1117/12.2533757
35. Y. Wang, W. Zhang, A. Cai, L. Wang, C. Tang, Z. Feng, et al., An effective sinogram inpainting for complementary limited-angle dual-energy computed tomography imaging using generative adversarial networks, *J. X-Ray Sci. Technol.*, **29** (2021), 37–61. https://doi.org/10.3233/XST-200736
36. M. Mirza, S. Osindero, Conditional generative adversarial nets, preprint, arXiv:1411.1784. https://doi.org/10.48550/arXiv.1411.1784
37. G. E. Hinton, R. R. Salakhutdinov, Reducing the dimensionality of data with neural networks, *Science*, **313** (2006), 504–507. https://doi.org/10.1126/science.1127647
38. P. Isola, J. Y. Zhu, T. Zhou, A. A. Efros, Image-to-image translation with conditional adversarial networks, in *IEEE Conference on Computer Vision and Pattern Recognition (CVPR)*, (2017), 1125–1134. https://doi.org/10.1109/CVPR.2017.632
39. K. Simonyan, A. Zisserman, Very deep convolutional networks for large-scale image recognition, preprint, arXiv:1409.1556. https://doi.org/10.48550/arXiv.1409.1556
40. A. Odena, C. Odena, J. Odena, Conditional image synthesis with auxiliary classifier GANs, in *The 34th International Conference on Machine Learning*, **70** (2017), 2642–2651.
41. C. A. Micchelli, L. Shen, Y. Xu, Proximity algorithms for image models: denoising, *Inverse Probl.*, **27** (2011), 045009. https://doi.org/10.1088/0266-5611/27/4/045009

42. M. Ljungberg, S. E. Strand, M. A. King, *Monte Carlo Calculations in Nuclear Medicine: Applications In Diagnostic Imaging*, CRC Press, 2012. https://doi.org/10.1201/b13073
43. M. Morphis, J. Staden, H. D. Raan, M. Ljungberg, Modelling of energy-dependent spectral resolution for SPECT Monte Carlo simulations using SIMIND, *Heliyon*, **7** (2021), e06097. https://doi.org/10.1016/j.heliyon.2021.e06097
44. S. Peltonen, U. Tuna, E. Sanchez-Monge, U. Ruotsalainen, PET sinogram denoising by block-matching and 3D filtering, in *2011 IEEE Nuclear Science Symposium Conference Record*, (2011), 3125–3129. https://doi.org/10.1109/NSSMIC.2011.6152568


AIMS Press